Supporting Information

Controlling Catalyst-Semiconductor Contacts: Interfacial Charge Separation in p-InP Photocathodes

Aaron J Kaufman, Raina A Krivina, Meikun Shen, Shannon W Boettcher*
Department of Chemistry and Biochemistry, University of Oregon, 97403, USA
E-mail: swb@uoregon.edu

Experimental Section/Methods

Photocathode preparation: All semiconductor substrates used in this study were cut from single-side-polished Zn-doped p-InP ($N_a = 4.2 \times 10^{17}$ cm^{-3}) from MTI. Ohmic back contacts were fabricated by thermally evaporating Au (20 nm)/Zn (30 nm)/Au (50 nm) on the unpolished p-InP face and annealing at 450 °C for 90 s in air. A small shadow mask was used to create two disconnected backside contacts to ensure ohmic current-voltage response through the backside to the p-InP.

Electrodes were fabricated using a Sn–Cu wire (length ~20 cm, –30 American wire gauge, McMaster Carr) electrically connected to the ohmic back contact by Ag paint (Ted Pella, Inc), fed through a glass tube. All but the active region of the electrode was encapsulated in epoxy. The electrodes were pretreated with conc. aq. HCl (Fisher) until rapid gas evolution was observed) or H_2O_2/HCl (5 min etch 0.25 м H_2O_2 (Fisher)/1 м HCl followed by a 15 sec etch in 2 м HCl), rinsed with water (18.2 MΩ cm) and dried with and N_2 gas stream.

A Bio-Logic SP300 potentiostat was used to electrodeposit Pt on the p-InP electrodes. A solution of 0.5 M Na_2SO_4 / 4 mM H_2PtCl_6 in water (18.2 MΩ cm) was used for electrodeposition. Pt was deposited at -0.15 V vs. SCE (standard calomel electrode, Accumet) with a Pt wire coil counter electrode under illumination of 100 mW cm^{-2} solar simulation (Abet Technologies, 10500) until the predetermined amount of charge had passed. Prior to insertion of the photocathode, the deposition solution was sparged with N_2 for 15 min to remove dissolved O_2. The deposition time was controlled by integrated current density, 5, 30, 100 mC cm^{-2} to create various particle densities. The electrodes were rinsed with water (18.2 MΩ cm) and dried with N_2. For some electrodes, instead 40 nm of Pt was deposited by physical vapor deposition (AMOD, Angstrom Engineering).

Electrochemical measurements: A Bio-Logic SP300 potentiostat was used to measure the electrochemical behavior of the photocathodes. The electrolyte was aq. 1 ᴍ $HClO_4$ (JT Baker Chemical Co.) saturated with H_2 by bubbling. Illuminated cyclic voltammograms, with a ramp rate of 20 mV/s, were carried out in an electrochemical cell with an SCE reference electrode and a Pt wire coil counter electrode in a separate chamber separated by a glass frit. The electrolyte was rapidly stirred to remove H_2 bubbles formed with custom stirring high-speed apparatus. The photocathode was illuminated with ~100 mW cm^{-2} of solar simulation, measured by a photodiode (ThorLabs UDT UV-005). Current densities were calculated from the total active region of each electrode determined using a calibrated digital scanner.

Dual-working-electrode (DWE) measurements used the second channel on the SP300 potentiostat, fitted with an ultra-low current module, to control the second working electrode attached to the catalyst layer. Reference electrode leads from both channels were shorted to the same SCE electrode in the 1 ᴍ $HClO_4$. Similarly, the counter-electrode leads were also shorted to the same Pt-wire-coil counter electrode.

The fabrication procedure for the DWE electrodes follows that detailed above, except Pt was deposited by PVD after electrode preparation. Sn–Cu wire was electrically connected to this film by Ag paint and all but the active area was encased in epoxy to avoid shorts and to precisely define the geometric active area.

Electron Beam Lithography and AFM measurements: Effective removal of the native oxide was critical for EBL samples. The samples were rinsed with acetone, isopropyl alcohol, and H_2O while mounted the spin coater (Headway Research), and spun dry after each step (3000 rpm for 60 s). A solution of 0.25 ᴍ H_2O_2 / 1 ᴍ HCl was placed on the substrate for a 5 min etch followed by a 15 s etch in 2 ᴍ HCl, and then spun to dry after each step.

The electron-beam resist (CSAR AR-P-6200.4, Allresist) was pulled into a syringe and warmed to room temperature prior to deposition. The resist was then dropped on the substrate to cover the sample completely and spun at 3000 rpm for 60 s. A soft bake at 150 °C was performed for 1 min to solidify the tacky film. This procedure produced resist films of 100 nm in thickness, measured by stylus profilometry (Veeco Dektak 6M).

EBL patterns were coded in NPGS (JC Nabity) and written using a ThermoFisher Apreo S2 SEM. The nanodisks were written at 5 kV with a beam current of 50 pA (43.1 pA measured) to increase scattering events inside the resist. Point exposures ranging from 1 to 50 fC was used to define dots with 1 um center-to-center pitch

The exposed samples were developed in AR 600-548 at 0 °C in an ice bath for 1 min. The samples were promptly rinsed with water (18.2 MΩ cm) and dried with N_2. The developed samples were metalized with 5 nm or 8 nm of Pt, deposited at 0.5 Å/s by electron-beam deposition. Lift-off was performed with dichloromethane (DCM, Sigma Aldrich) by soaking for 5 min. Agitation was performed during the soak by jets of DCM with a needle and syringe to facilitate liftoff.

A Bruker Dimension ICON with ScanAsyst was used for topographical AFM and C-AFM measurements, using the onboard SMU. SCM-PIT-V2 probes were used for all measurements. Both electrodeposited Pt nanoparticles and EBL-defined Pt nanodisks were analyzed by the C-AFM.

XPS and TEM: All samples analyzed by X-ray photoelectron spectroscopy (XPS) used an ESCALAB 250 (ThermoScientific) and an Al $K\alpha$ monochromated source (20 eV pass energy), 500 μm spot size). The samples were charge-neutralized using an in-lens electron source. Spectra were analyzed using ThermoScientific Avantage 4.88 software. The adventitious C 1s signal at 284.8 eV was used to calibrate the binding-energy scale.

A FEI Titan 80-200 TEM/STEM with ChemiSTEM was used for collecting the data at 200 kV in Figure 5. TEM Lamella was prepared on a dual-beam FEI Helios and milled with Ga ions. The selected areas were coated with 100 nm of electron-beam-deposited carbon and then 1000 nm of ion-beam-deposited carbon to protect the interface during imaging.

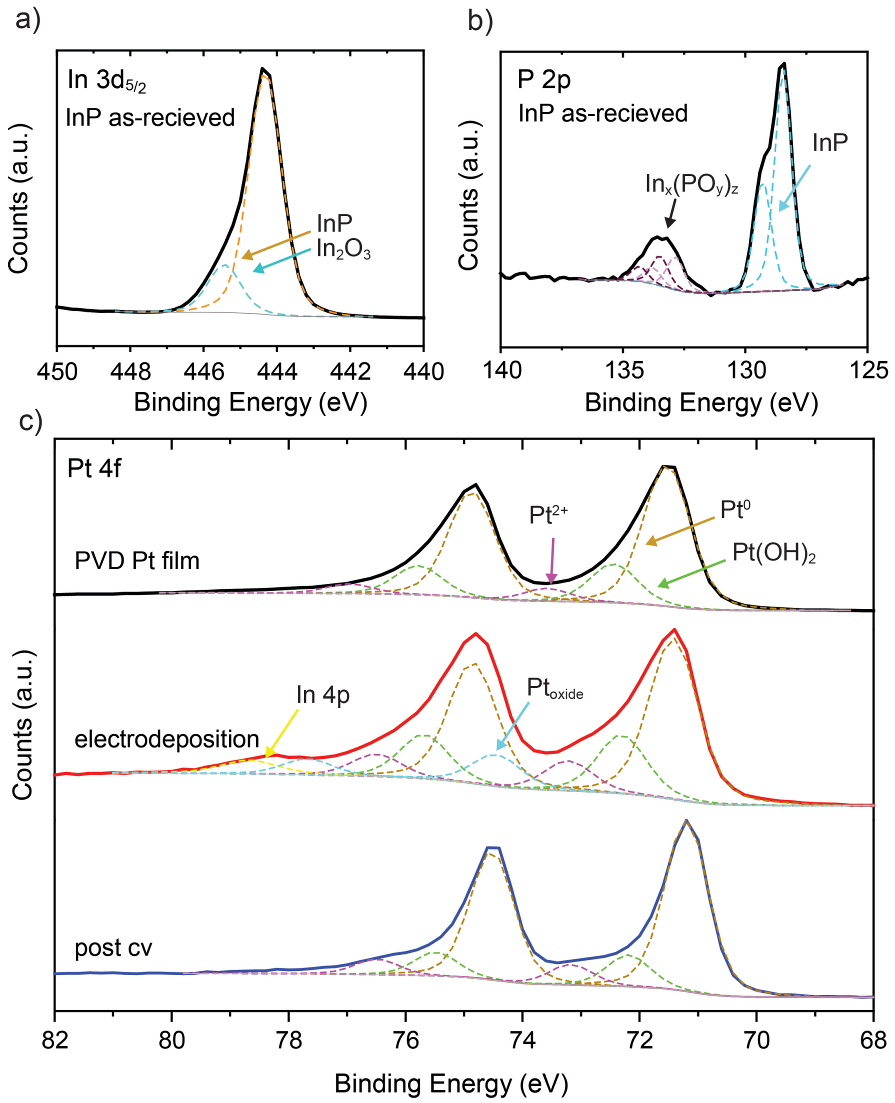

Figure S1 a) and b) XPS spectra of In $3d_{5/2}$ and P 2p of "as-received" InP. c) Pt 4f XPS spectra of an as-deposited 40-nm-thick Pt film on p-InP (top), electrodeposited Pt atop an H_2O_2/HCl pretreated p-InP surface (middle), and electrodeposited Pt after electrochemical cycling (one dark cycle and five illuminated cycled in 1 м $HClO_4$) All Pt 4f spectra were fit with sets of doublets except for the electrodeposited Pt sample where a singlet corresponding to In 4p state was added at 78.7 eV to account for the overlap in energy between Pt 4f and In 4p.

Table S1: In $3d_{5/2}$ spectra peak positions for all samples in the manuscript.

Source	In $3d_{5/2}$ (eV)					
	InP	InO_x	$InPO_x$	$In(PO_3)_3$	$In(PO_3)$	$InPO_4$
literature	444.3[1–5]	444.9[1–4]	/	445.4[1–4]	445.5[2]	445.7[1,4,5]
H_2O_2/HCl etch	444.5	445.3	/	/	/	/
e-dep Pt	445	445.8	446.4	/	/	/
e-dep Pt, CV	444.9	445.8	/	/	/	/
EBL Pt, CV	444.2	445.3	/	/	/	/
as-received	444.3	445.1	445.7	/	445.7	/

Table S2 P 2p spectra peak positions for all samples in the manuscript.

Source	**P 2p (eV)**					
	InP	InP_{surf}	$In(PO_3)$	$InPO_4$	$In(PO_3)_3$	P_2O_5
literature	128.8[2–6]	129.06[5]	133.5[2,6]	133.81[1,3–5]	134.3[1,4,7]	135.0[1,2]
H_2O_2/HCl etch	128.5	129.0	132.1	132.8	/	/
e-dep Pt	129.0	129.8	132.6	133.3	133.9	/
e-dep Pt, CV	128.9	129.6	132.5	133.2	133.8	/
EBL Pt, CV	128.5	129.2	132.5	133.1	/	/
as-received	128.4	/	132.8	133.5	/	/

Table S3 In$3d_{5/2}$ spectra atomic percent of each species present relative to the total amount of that element in each spectra for all samples in the manuscript.

Source	**In $3d_{5/2}$**		
	InP	InO_x	$InPO_x$
H_2O_2/HCl etch	91.0%	9.0%	/
e-dep Pt	61.7%	27.6%	10.8%
e-dep Pt, CV	86.6%	13.4%	/
EBL Pt, CV	84.0%	16.0%	/
as-received	76.8%	15.6%	7.6%

Table S4: P 2p atomic percent of each species present relative to the total amount of that element in each spectra for all samples in the manuscript from XPS analysis.

Source	**P 2p**				
	InP	InP_{surf}	$In(PO_3)$	$InPO_4$	$In(PO_3)_3$
H_2O_2/HCl	85.6%	6.5%	3.5%	4.4%	/
eDep	51.1%	2.6%	13.7%	15.8%	16.8%
eDep CV	76.6%	7.1%	4.9%	5.8%	5.7%
EBL CV	72.9%	8.8%	8.1%	10.3%	/
As-Received	77.1%	/	10.8%	12.1%	/

Additional Discussion. H_2O_2/HCl pretreatment removes phosphorus oxides and In_2O_3 from the as-received sample as is evidenced by comparing InP peaks (substrate) in both the In $3d_{5/2}$ (Table S3) and the P 2p (Table S4) spectra. Physical-vapor-deposited Pt on top of H_2O_2/HCl pretreated p-InP is considered, within this work, a "pristine" Pt/p-InP junction. This pristine junction was observed to have ohmic (linear) current-voltage response, as simple Schottky-contact models predict (Figure S4). EBL-defined Pt nanodisks were subject to an H_2O_2/HCl pretreatment before electron-beam deposition of Pt, yielding a nearly pristine junction between Pt and p-InP. A thin native oxide is likely to have grown around the nanodisks, however, before dry C-AFM measurements were conducted in air which we hypothesize leads to pinch-off effects.[8–10] After undergoing one dark CV (-0.3 to 0.5 V vs SCE) in 1 M $HClO_4$ and 5 illuminated CV cycles (-0.3 to 0.6 V vs SCE), with one sun equivalent illumination, In and P oxides were observed in a greater degree than in the H_2O_2/HCl pretreated p-InP sample (Figure 1, Table S3 and Table S4). XPS spectra of a sample with a 40 nm Pt film on p-InP displayed in Figure S1c., was shown to match that of the electrodeposited (edep) Pt after photoelectrochemical cycling in 1 M $HClO_4$, indicating that a permanent change in the composition of Pt is likely not the dominant mechanism for the formation of the charge-selective junction. The presence of oxides in the photoelectrodeposited Pt samples was observed in high percentages immediately after deposition (Table S3 and Table S4). TEM images of the Pt nanodisk sample (Figure 5) after photoelectrochemical cycling (one dark, five light CVs) indicate that the amorphous oxide grew underneath the nanodisk, apparently forming an electrical heterojunction.

Samples containing electrodeposited Pt displayed a binding-energy shift, to higher binding energy, for the peaks in the In $3d_{5/2}$ and P 2p spectra. However, this shift is not observed in the Pt 4f spectra nor in Figure 5b. Therefore, we propose the shift to higher binding energies was primarily caused by surface charging effects with the presence of electrodeposited Pt. Although, band bending may also contribute to the spectral shift observed in some samples. The subsequent species peak identification was appropriately adjusted.

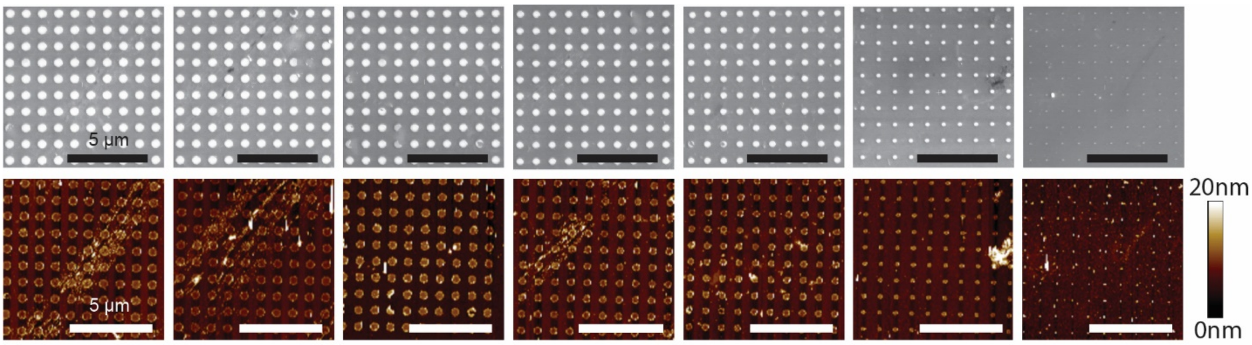

Figure S2: SEM micrographs (top) and AFM topographical maps (bottom) of the same EBL defined Pt nanodisk arrays (vertically aligned), scale bars indicate 5000 nm.

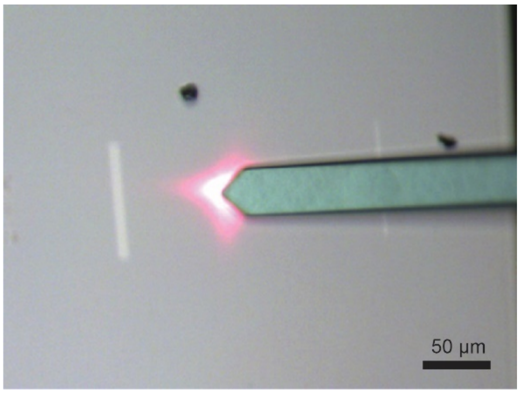

Figure S3: Bruker SCM-PIT Pt-Ir coated cantilever engaged with the electrode surface. Illumination for C-AFM experiments was created by the onboard laser light spillover (690 nm) creating ~ 5 sun intensity, estimated with a Thor Labs UDT UV-005 photodiode. Dark C-AFM measurements were conducted with the laser spot located near the aft end of the cantilever, ~400 µm away from the area of interrogation.

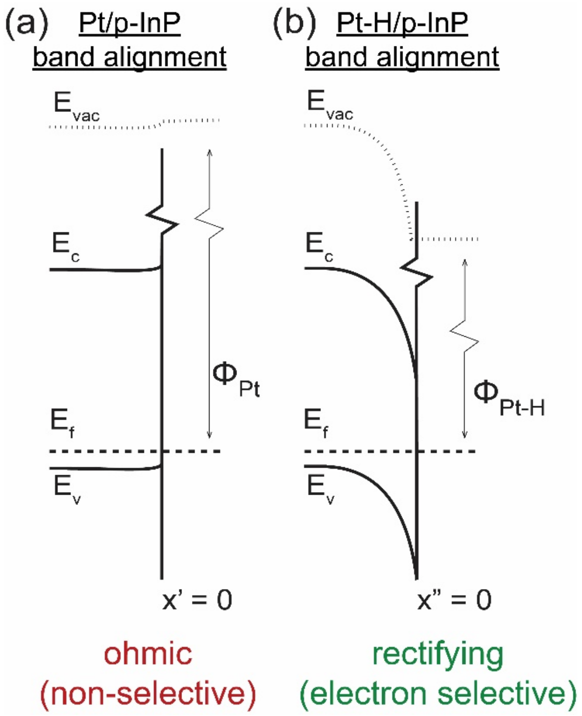

Figure S4: (a) Schematic band alignment for Pt/p-InP based on conventional Schottky-junction models, and (b) hypothesized band alignment and barrier created in the adaptive junction picture (H_2 absorption).

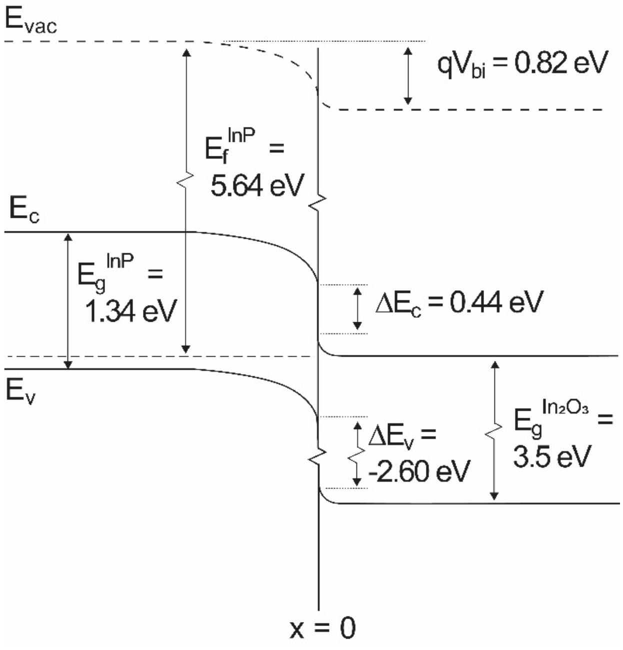

Figure S5: Heterojunction band alignment schematic with reported energy values adopted from Leibovitch and modified for the p-InP used in this study.[11] Using 1.1×10^{21} cm^{-3} as the effective density of states for p-InP, the distance from the valence band maximum (E_v) and the Fermi level (E_f) would be 0.084 eV. Therefore, the expected barrier for this heterojunction is 0.904 eV. E_c and E_g denote the conduction band energy and the bandgap, respectively.

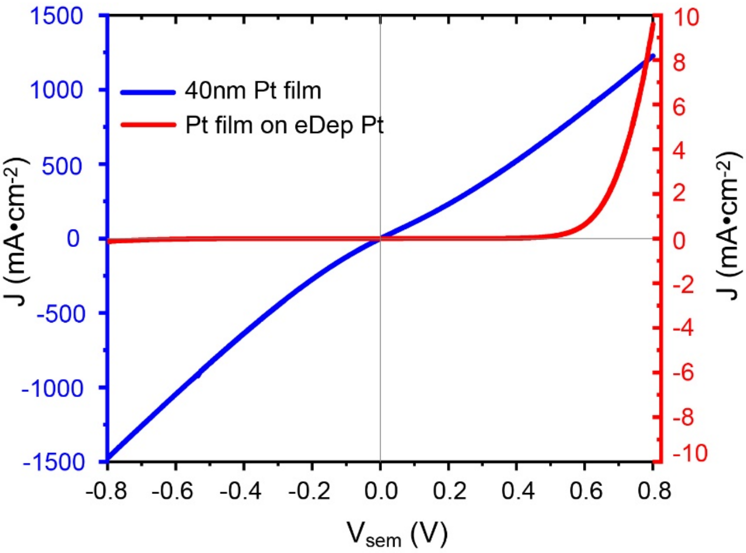

Figure S6: Dry two-electrode *J-V* curves of 40-nm Pt film on freshly etched InP (blue and left axis) compared with a sample with 40 nm Pt film by PVD deposited on 5 mC cm^{-2} electrodeposited Pt/p-InP. The Pt film on the freshly etched InP displays ohmic behavior whereas the same PVD Pt film on the electrodeposited Pt/p-InP displays rectifying behavior. Forward bias corresponds to positive potentials applied to the semiconductor ohmic back contact relative to the Pt top contact.

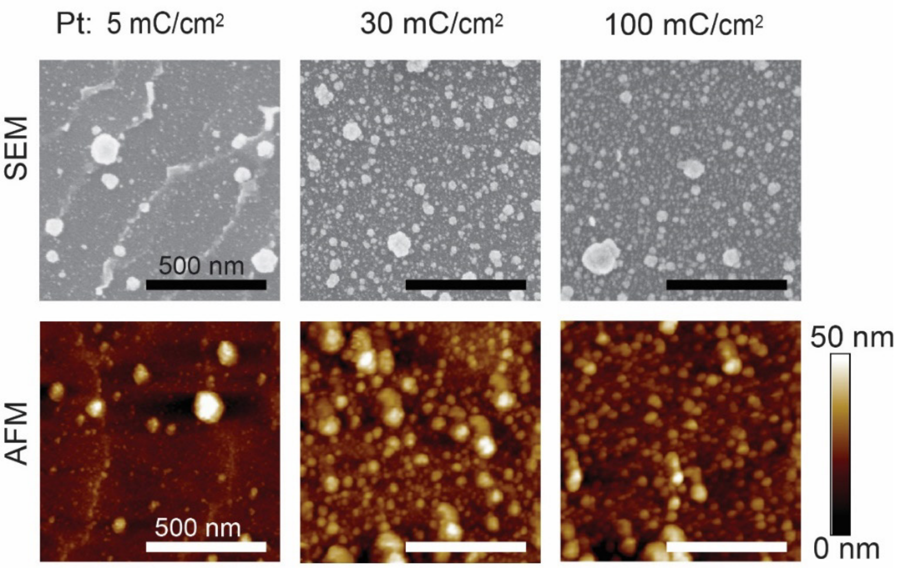

Figure S7: SEM micrographs (top) and AFM topography maps (bottom) of electrodeposited Pt with integrated current densities at 5, 30, and 100 mC cm^{-2}. SEM and AFM maps are vertically aligned with different regions on the same electrode and the scale bars are all the same size.

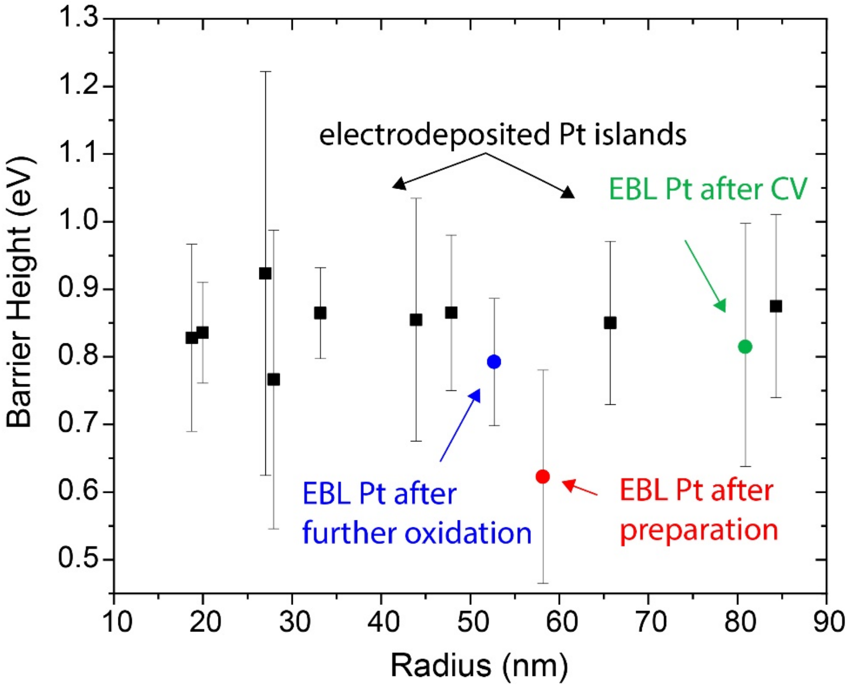

Figure S8: Barrier height calculations from electrodeposited nanoparticles and EBL-defined Pt nanodisks of comparable size on p-InP.

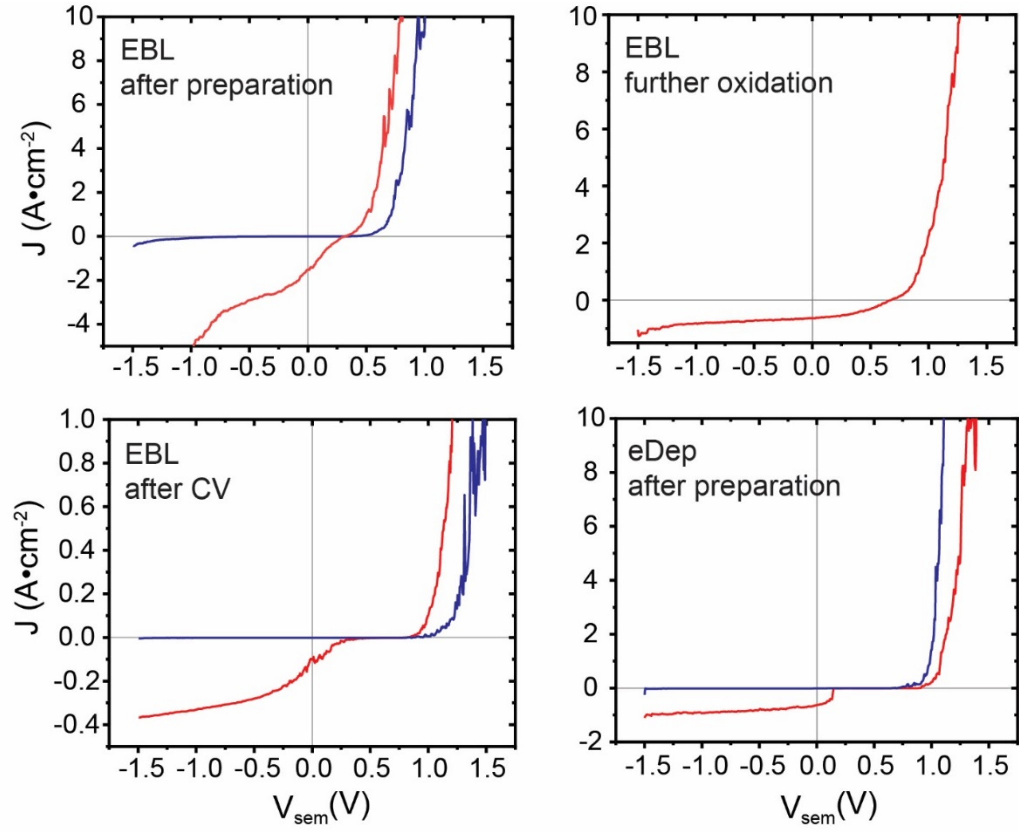

Figure S9: Example C-AFM current response to voltage ramps of nanoscale contacts in air under the dark conditions (blue) and under 5 suns equivalent illumination (red) by the onboard 690 nm laser.

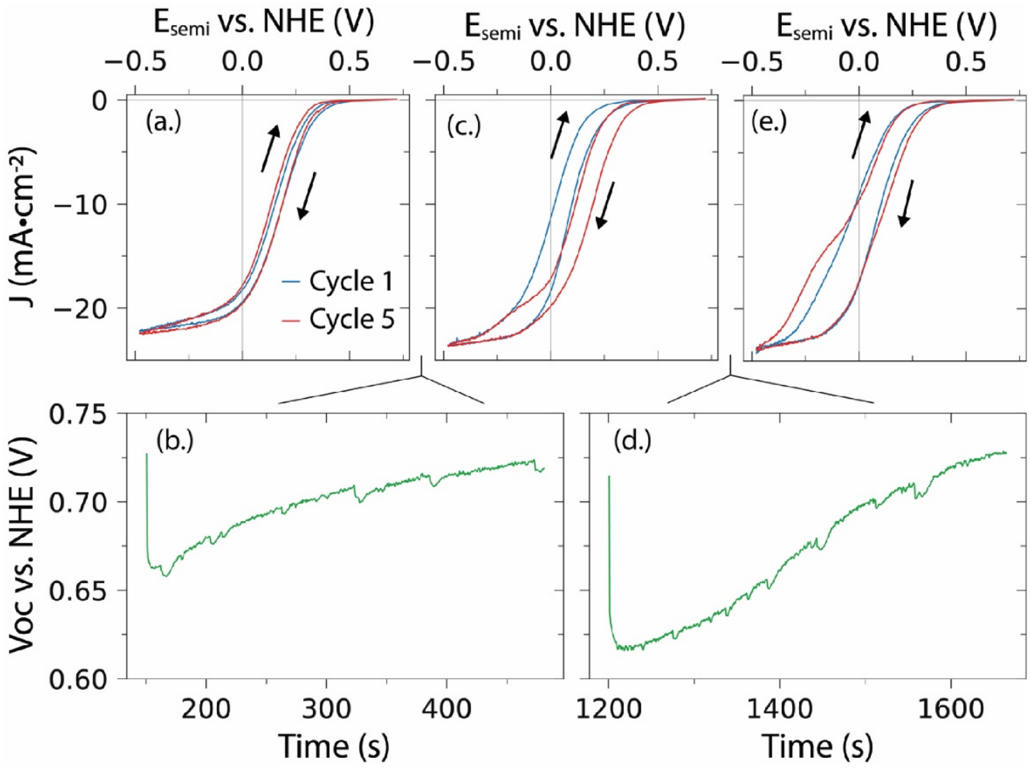

Figure S10: Open-circuit voltage (V_{oc}) degradation and recovery. Electrodeposited Pt (30 mC cm^{-2})/p-InP photocathodes were cycled in 1 M $HClO_4$ and illuminated with 1 sun equivalent light intensity. Three CV experiments each of 5 cycles (a, c, e) were sequentially conducted with irradiated open-circuit voltage data collected in between each of the CV experiments (b, d). The first data points in plots (b) and (d) are artifacts from the end of the previous scan, ending at the initial open-circuit voltage. The open-circuit voltage recovery is evident when the sample is sitting at open circuit under illumination, presumably due to the formation/recovery of the interfacial oxide that creates the charge selective heterojunction.

Pinch-off Discussion: A Pt/p-InP "pristine" contact may become pinched-off if the contact's lateral dimension is on the order of the depletion width of a higher-barrier-forming peripheral n-type oxide grown in air.[8,10] In the case of pinched-off particles which begin to grow a thin interfacial oxide, the thin n-type oxide interlayer, fully depleted by Pt, may still display the pinch-off effect albeit to a lesser degree due to shielding. Nonetheless, the electronic transport behavior of such pinched-off contacts can be described by Tung's patch theory, Equation S1.[8,9] This theoretical transport equation resembles that of the familiar Schottky diode equation with a barrier correction term (C_b, describing the radially inhomogeneous barrier height) and an area correction term (C_a, describing the radially inhomogeneous current densities).

$$\mathrm{I_{patch}} = \mathrm{A^*\,T^2\,C_a}\exp\left(\frac{\phi_b^0}{\mathrm{k_BT}} + C_b\right)\left(\exp\left(\frac{\mathrm{qV_{app}}}{\mathrm{nk_BT}}\right) - 1\right) \tag{S1}$$

$$C_a = \frac{4\pi k_BT}{9q}\left(\frac{3\Delta r^2}{4}\right)^{\frac{1}{3}}\left(\frac{\epsilon_s}{qN_AV_{bb}}\right)^{2/3} \tag{S2}$$

$$C_b = \frac{q}{k_BT}\left(\frac{3q\Delta r^2N_AV_{bb}}{4\epsilon_s}\right)^{1/3} \tag{S3}$$

Pinch-off is seen on disk (particle) size scales of $\frac{\Delta}{V_{bb}} > \frac{2r}{W}$, where W is the width of the depletion region given by $\sqrt{\frac{2\epsilon_s V_{bb}}{qN_A}}$ and $V_{bb} = \phi_b^0 - V_n - V_{app}$, Δ is the difference in barrier height between the patch and the periphery (ϕ_b^0) and V_n is the difference between the conduction band minimum and the Fermi level. Since the barrier between Pt and pristine p-InP ($N_A = 4.3\times10^{17}$ cm^{-3}) is considered to be zero and the peripheral barrier is thought to be 1 eV (In_2O_3/p-InP), $\frac{\Delta}{V_{bb}} \approx 1$.

Illuminated nanocontacts which generate photocurrent, in turn, develop an open-circuit voltage vs. the ohmic back contact. Solving Equation S1 for the open-circuit voltage yields,

$$qV_{oc} = nk_BT \ln\left(\frac{J_{ph}A\{r\}}{A^*\,T^2\,C_a\{r\}\,exp\left(\frac{\phi_b^0}{k_BT}+C_b\{r\}\right)} + 1\right) \tag{S4}$$

Heterojunction Schottky-like barrier discussion: Due to the high expected electron concentration in In_2O_3, we assume the junction approaches the Mott-Schottky metal/semiconductor limit and can be effectively modeled by the ideal diode equation, Equation S5.

$$J = J_0\left(\exp\left(\frac{qV_{app}}{nk_BT}\right) - 1\right) \tag{S5}$$

$$J_0 = A^*T^2\exp\left(-\frac{\varphi_b}{k_BT}\right) \tag{S6}$$

$$qV_{oc} = nk_BT\ \ln\left(\frac{J_{ph}}{J_0} + 1\right) \tag{S7}$$

Since $\frac{J_{ph}}{J_0}$ is typically >>1, $qV_{oc} = nk_BT\ln(\mathrm{J_{ph}}) + nk_BT\ln\,(A^*T^2)\,\frac{\varphi_b}{k_BT}$, we can see the relationship of V_{oc} and the junction barrier height. Of course, ln(J_{ph}) also is a function of the barrier height however this parameter influences qV_{oc} to a lesser degree when moderately perturbed from a non-zero φ_b.

Transport properties: A non-selective, ohmic junction, is expected for the pristine Pt and p-InP interface. This was observed for 40-nm Pt films deposited by physical vapor deposition on H_2O_2/HCl pretreated p-InP. Additionally, large-radius Pt nanodisks defined by EBL were observed to be non-selective (Figure 4b), in accordance with pinch-off theory.[8–10,12] Non-selective Pt/InP interfaces were observed to develop a reversible small barrier in Figure 2b when the 40-nm Pt films were exposed to an H_2-rich atmosphere. This behavior has been attributed to the formation of a small interfacial dipole in Pt (and Pd) H_2-gas-sensing devices and measured in Figure 3c to increase the interfacial barrier by ~50 meV.[13,14] An irreversible transformation from ohmic to rectifying was observed in Figures 3c and 4b where a significant energetic barrier was established (~0.93 eV) and (~0.83 eV) after electrochemically cycling under irradiation in 1 M $HClO_4$.

Pt nanoparticles deposited by electrodeposition were observed to immediately be rectifying in Figure S9. Figure S8 shows that electrodeposited particles have a barrier height independent of radius. Additionally, energy barrier heights calculated for the EBL-defined nanodisks, post-electrochemical cycling, and EBL nanodisks, following further oxidation in room temperature air, all display the same barrier height (within one standard error). Barrier heights calculated from the DWE experiment (40 nm Pt film) in the Figure 3b inset, fall within the standard error of ex situ dry barrier heights in Figure S7.

Macroscopic CV scans of electrodeposited Pt nanoparticles display tunnel junction behavior for photoelectrodes with low Pt loading. Smaller particles are more susceptible to the effects of undercutting by a peripheral nonconductive oxide. Increased tunnel junction behavior was observed in Pt/p-InP on electrode particles and in EBL-defined nanodisks after photoelectrochemistry. This behavior can be observed in the illuminated *J-V* curves recorded by C-AFM in Figure S9 where large resistances were observed in the illuminated *J-V* curves at V_{oc}. Transitions in electronic properties and electron densities in the complex oxide and may be attributed to the population and removal of oxygen vacancies along with the chemical transition of the oxide to liberated protons during photo-electrochemistry.[15,15–18]

References

(1) Hollinger, G.; Bergignat, E.; Joseph, J.; Robach, Y. On the Nature of Oxides on InP Surfaces. *Journal of Vacuum Science & Technology A* **1985**, *3* (6), 2082–2088. https://doi.org/10.1116/1.572928.

(2) Hussey, R. J.; Sproule, G. I.; McCaffrey, J. P.; Graham, M. J. Characterization of Oxides Formed on InP, InGaAs, InAlAs, and InGaAs/InAlAs Heterostructures at 300–500°C. *Oxidation of Metals* **2002**, *57* (5), 427–447. https://doi.org/10.1023/A:1015396204143.

(3) Muñoz, A. G.; Heine, C.; Lublow, M.; Klemm, H. W.; Szabó, N.; Hannappel, T.; Lewerenz, H.-J. Photoelectrochemical Conditioning of MOVPE P-InP Films for Light-Induced Hydrogen Evolution: Chemical, Electronic and Optical Properties. *ECS J. Solid State Sci. Technol.* **2013**, *2* (4), Q51–Q58. https://doi.org/10.1149/2.016304jss.

(4) Faur, M.; Faur, M.; Jayne, D. T.; Goradia, M.; Goradia, C. XPS Investigation of Anodic Oxides Grown on P-Type InP. *Surface and Interface Analysis* **1990**, *15* (11), 641–650. https://doi.org/10.1002/sia.740151102.

(5) Cuypers, D.; van Dorp, D. H.; Tallarida, M.; Brizzi, S.; Conard, T.; Rodriguez, L. N. J.; Mees, M.; Arnauts, S.; Schmeisser, D.; Adelmann, C.; De Gendt, S. Study of InP Surfaces after Wet Chemical Treatments. *ECS J. Solid State Sci. Technol.* **2014**, *3* (1), N3016–N3022. https://doi.org/10.1149/2.005401jss.

(6) Hofmann, A.; Streubel, P.; Meisel, A. XPS Investigation of Oxide Films on InP(100). *Surf. Interface Anal.* **1988**, *12* (5), 315–319. https://doi.org/10.1002/sia.740120508.

(7) Faur, M.; Faur, M.; Jenkins, P.; Goradia, M.; Bailey, S.; Jayne, D.; Weinberg, I.; Goradia, C. Study of Surface Passivation of InP. *Surf. Interface Anal.* **1990**, *15* (12), 745–750. https://doi.org/10.1002/sia.740151207.

(8) Tung, R. T. Electron Transport at Metal-Semiconductor Interfaces: General Theory. *Phys. Rev. B* **1992**, *45* (23), 13509–13523. https://doi.org/10.1103/PhysRevB.45.13509.

(9) Tung, R. T. Electron Transport of Inhomogeneous Schottky Barriers. *Appl. Phys. Lett.* **1991**, *58* (24), 2821–2823. https://doi.org/10.1063/1.104747.

(10) Laskowski, F. A. L.; Oener, S. Z.; Nellist, M. R.; Gordon, A. M.; Bain, D. C.; Fehrs, J. L.; Boettcher, S. W. Nanoscale Semiconductor/Catalyst Interfaces in Photoelectrochemistry. *Nature Materials* **2020**, *19* (1), 69–76. https://doi.org/10.1038/s41563-019-0488-z.

(11) Leibovitch, M.; Kronik, L.; Fefer, E.; Korobov, V.; Shapira, Y. Constructing Band Diagrams of Semiconductor Heterojunctions. *Appl. Phys. Lett.* **1995**, *66* (4), 457–459. https://doi.org/10.1063/1.114055.

(12) Tung, R. T. The Physics and Chemistry of the Schottky Barrier Height. *Applied Physics Reviews* **2014**, *1* (1), 011304. https://doi.org/10.1063/1.4858400.

(13) Lundström, I.; DiStefano, T. Hydrogen Induced Interfacial Polarization at Pd-SiO_2 Interfaces. *Surface Science* **1976**, *59* (1), 23–32. https://doi.org/10.1016/0039-6028(76)90288-0.

(14) Armgarth, M.; Söderberg, D.; Lundström, I. Palladium and Platinum Gate Metal-oxide-semiconductor Capacitors in Hydrogen and Oxygen Mixtures. *Appl. Phys. Lett.* **1982**, *41* (7), 654–655. https://doi.org/10.1063/1.93638.

(15) Van de Walle, C. G.; Neugebauer, J. Universal Alignment of Hydrogen Levels in Semiconductors, Insulators and Solutions. *Nature* **2003**, *423* (6940), 626–628. https://doi.org/10.1038/nature01665.

(16) Gu, Z.; Zhang, L.; Wen, B.; An, X.; Lan, H.; Liu, L.-M.; Chen, T.; Zhang, J.; Cao, X.; Tang, J.; Liu, H.; Qu, J. Efficient Design Principle for Interfacial Charge Separation in Hydrogen-Intercalated Nonstoichiometric Oxides. *Nano Energy* **2018**, *53*, 887–897. https://doi.org/10.1016/j.nanoen.2018.09.019.

(17) Kumar, M.; Chatterjee, R.; Milikisiyants, S.; Kanjilal, A.; Voelskow, M.; Grambole, D.; Lakshmi, K. V.; Singh, J. P. Investigating the Role of Hydrogen in Indium Oxide Tubular Nanostructures as a Donor or Oxygen Vacancy Passivation Center. *Appl. Phys. Lett.* **2009**, *95* (1), 013102. https://doi.org/10.1063/1.3159786.

(18) King, P. D. C.; Lichti, R. L.; Celebi, Y. G.; Gil, J. M.; Vilão, R. C.; Alberto, H. V.; Piroto Duarte, J.; Payne, D. J.; Egdell, R. G.; McKenzie, I.; McConville, C. F.; Cox, S. F. J.; Veal, T. D. Shallow Donor State of Hydrogen in In_2O_3 and SnO_2: Implications for Conductivity in Transparent Conducting Oxides. *Phys. Rev. B* **2009**, *80* (8), 081201. https://doi.org/10.1103/PhysRevB.80.081201.